crystals

MDPI

Article

The Synthesis and Domain Structures of Single-Crystal-Like Mesoscale $BaTiO_3$ Plates

Kun Zheng [1], Jian Zhuang [1,*], Yi Quan [2], Jinyan Zhao [1], Lingyan Wang [1], Zhe Wang [1] and Wei Ren [1,*]

[1] Electronic Materials Research Laboratory, Key Laboratory of the Ministry of Education & International Center for Dielectric Research, School of Electronic Science and Engineering, Xi'an Jiaotong University, Xi'an 710049, China
[2] School of Microelectronics, Xidian University, Xi'an 740071, China
* Correspondence: jzhuang@xjtu.edu.cn (J.Z.); wren@mail.xjtu.edu.cn (W.R.)

Abstract: The (001) plate-like $BaTiO_3$ piezoelectric micromaterials are synthesized by topochemical microcrystal conversion technique. $BaTiO_3$ plates with a length of 2~10 μm and thickness of 0.5~1.3 μm are obtained. The dependence of morphology on synthesis conditions is discussed in detail. The crystal symmetry and multiscale domain structures of $BaTiO_3$ plates are systematically investigated by various characterizations. X-ray diffraction (XRD) and Raman spectra analyses demonstrate the tetragonal symmetry of the (001) oriented $BaTiO_3$ plates at room temperature. The domain configurations of the micron $BaTiO_3$ are investigated with a polarized light microscope (PLM) and piezoresponse force microscopy (PFM). The single-crystal-like quality and uniformity are supported by PLM observations. More importantly, the classical 90° banded ferroelectric domains of ~125 nm width are observed for the first time in such $BaTiO_3$ plates. The domain features in the mesoscale $BaTiO_3$ plate are discussed and compared with its bulk counterparts. The results may provide insights into understanding and designing the mesoscale $BaTiO_3$ functional materials.

Keywords: $BaTiO_3$; mesoscale; topochemical microcrystal conversion; domain structure; perovskite

Citation: Zheng, K.; Zhuang, J.; Quan, Y.; Zhao, J.; Wang, L.; Wang, Z.; Ren, W. The Synthesis and Domain Structures of Single-Crystal-Like Mesoscale $BaTiO_3$ Plates. *Crystals* **2023**, *13*, 538. https://doi.org/10.3390/cryst13030538

Academic Editor: Pankaj Sharma

Received: 27 February 2023
Revised: 15 March 2023
Accepted: 15 March 2023
Published: 21 March 2023

1. Introduction

Barium titanate ($BaTiO_3$) is a classical lead-free ferroelectric/piezoelectric material that was first discovered in the early 1940s [1]. $BaTiO_3$ exhibits a cubic perovskite structure, which transforms into a tetragonal symmetry at the Curie point around 120 °C [2]. At room temperature, $BaTiO_3$ was widely investigated in various material forms including single crystal and ceramics since its discovery, due to its excellent piezoelectric/ferroelectric/dielectric performances at room temperature.

Materials can display very distinct and interesting properties when the dimensions change from three-dimension bulk [3–5] to low-dimension nanoscale [6]. Generally, microscale and nanoscale refer to 1–100 μm and 1–100 nm, respectively, whereas mesoscale is somewhere in between. Significant advantages could be expected from those materials. Piezoelectric micro-/nano- materials and related devices have attracted more and more interest in recent years due to their small size and easy integration [7–9]. Two-dimensional ZnO platelet and the array assembled by ZnO platelets show great advantages as integrated piezotronic transistors [7]. Nanostructured piezoelectrics, for example, $BaTiO_3$ were combined with polymer to form composite porous foam [8], which enhanced piezocatalysis due to the nanomaterial and the specific surface area. Moreover, nano- or mesoscale $BaTiO_3$ materials can also be used as templates for piezoelectric ceramic texturing [10,11], which can enhance piezoelectric performance significantly. As a piezoelectric catalyst, nano- and micro-$BaTiO_3$ particles were successfully utilized in wastewater degradation and H_2 production [12,13].

It is believed that the ferroelectricity/piezoelectricity of $BaTiO_3$ is critical to the desired functionalities, and how to synthesize good-quality mesoscale $BaTiO_3$ with good perfor-

mances is therefore in high demand. In contrast to bulk $BaTiO_3$ and nanoscale $BaTiO_3$ materials, mesoscale $BaTiO_3$ is far less investigated. Single crystalline mesoscale $BaTiO_3$ thin plates were first reported by Remeika in 1954 [14]. These clear, large size crystals have desired ferroelectric characteristics [15]. However, the potassium fluoride flux used during the growth of $BaTiO_3$ single crystal is environmentally harmful and will cause the corrosion of furnace refractories. An eco-friendly and commonly used approach to obtain plate-like $BaTiO_3$ is the topochemical microcrystal conversion (TMC) technique, which was first reported by Liu et al. [16]. In the TMC process, bismuth layer structure precursors transform to perovskite structure $BaTiO_3$ in molten salt. There are two TMC methods reported on the synthesis of $BaTiO_3$ plates, including the one-step TMC and the two-step TMC. The one-step TMC converts the $Bi_4Ti_3O_{12}$ precursor to $BaTiO_3$ directly. The two-step TMC converts $Bi_4Ti_3O_{12}$ to $BaBi_4Ti_4O_{15}$ first, and then obtains $BaTiO_3$ from the $BaBi_4Ti_4O_{15}$ precursor. With the topochemical reactions, the Ba^{2+} ions completely replace the Bi^{3+} ions in the precursor. Moreover, the plate-like morphology of the precursor, meanwhile, is maintained in the final products. $BaTiO_3$ plates synthesized by the TMC method show a quadrate shape and a high aspect ratio. The obtained $BaTiO_3$ particles are either single crystalline or polycrystalline, which is determined by the initial alignment after nucleation and the recrystallization process [17]. Much work has been focused on controlling the morphology of mesoscale $BaTiO_3$ plates, which is mainly related to the following three factors. The first important factor is the choice of a suitable Aurivillius precursor. The morphology of the precursor directly affects the morphology of the final product during topochemical conversion. The morphology of $BaTiO_3$ can be optimized by using a suitable precursor with a high aspect ratio, regular shape, and clean surface. Liu et al. utilized polycrystalline $BaBi_4Ti_4O_{15}$ as a precursor for the preparation of $BaTiO_3$ [16]. The plate-like and rectangular Aurivillius precursor of about 6~10 μm in length successfully converts to 5~10 μmperovskite $BaTiO_3$ micrometer plates. Fan et al. found the exfoliation of $BaTiO_3$ during TMC when they used $Bi_4Ti_3O_{12}$ precursor or polycrystalline $BaBi_4Ti_4O_{15}$ precursor [18]. The exfoliation resulted in irregular shape $BaTiO_3$ plates and some fine particles among the plates. As a result, single-crystalline $BaBi_4Ti_4O_{15}$ precursor [18] was reported to achieve uniform $BaTiO_3$ plates. The size of $BaTiO_3$ plates was also found to be closely related to the size of the precursor [19]. Micrometer and sub-micrometer $BaTiO_3$ can be derived from a micro- or sub-micro-precursor, respectively. The second factor is the suitable molten salts. NaCl, KCl, and $BaCl_2$ salts are the commonly used molten salts in the synthesis of $BaTiO_3$ plates by the TMC method [16–19]. $BaCl_2$-KCl molten salts systems are used in the transformation from $Bi_4Ti_3O_{12}$ to $BaBi_4Ti_4O_{15}$, because of their higher Ba^{2+} concentration to accelerate the growth of $BaBi_4Ti_4O_{15}$ [16]. The NaCl-KCl molten salt system is used in the conversion from $BaBi_4Ti_4O_{15}$ to $BaTiO_3$. The last factor is the removal process of the salts and the byproducts. The resultant of the two-step TMC reaction includes $BaTiO_3$ plate-like particles, salts, and residual Bi_2O_3. Salts can be easily removed after washing with deionized water several times. In order to remove the Bi_2O_3, an acid-washing process is needed with the reaction between Bi^{3+} and nitric acid (HNO_3). Zuo et al. [20] compared two different washing methods. It was found to be better to first remove the salts by deionized water, and then eliminate the residual Bi^{3+} by HNO_3.

On the one hand, potential applications are highly reliant on physical properties, such as piezoelectric and dielectric performances. On the other hand, the polar domain structures and corresponding dynamics can serve as an important extrinsic contribution to obtained electric properties. Therefore, the investigation of domain features is critical to the understanding of physical behaviors. However, the domain structure of $BaTiO_3$ within the mesoscale is rarely reported. Wu et al. [13] reported PFM results of individual $BaTiO_3$ plates. Though the amplitude butterfly loop and phase hysteresis loop were obtained along the out-of-plane direction, no obvious domains can be seen. Kržmanc et al. [19] found irregular domains in the PFM results of $BaTiO_3$ plates, but the plates were stacked and the influence of polishing treatment cannot be ruled out.

In this work, we have optimized the synthesis of $BaTiO_3$ plates by the TMC method, which guarantees the obtainment of single-crystal-like $BaTiO_3$ materials in mesoscale. The crystal structure and microstructure of $BaTiO_3$ plates are determined using X-ray diffraction (XRD), Raman spectra, and field-emission scanning electron microscope (FE-SEM). More importantly, direct observation of the domain structures in the $BaTiO_3$ plates is performed by polarized light microscope (PLM) and piezoresponse force microscopy (PFM). The good quality sample enables the observation of clear domain configurations. The domain features of $BaTiO_3$ materials in mesoscale are discussed by comparing them with their bulk counterparts. The results may provide new insights into understanding and designing the mesoscale $BaTiO_3$ functional materials.

2. Materials and Methods

2.1. The Synthesis of the Precursors and the $BaTiO_3$ Plates

The $BaTiO_3$ plates were prepared by the TMC method in three steps. First, a stoichiometric amount of Bi_2O_3 (99%) and TiO_2 (98%) with respect to the $Bi_4Ti_3O_{12}$ precursor were mixed by ball milling in ethanol for 15 h. The mixture was then dried and calcined under 1080~1160 °C using an equal weight of molten salts. The molar ratio of NaCl (99.5%) and KCl (99.5%) salts was 1:1. Subsequently, $BaBi_4Ti_4O_{15}$ precursor particles were synthesized in 1:1 mol $BaCl{\cdot}2H_2O$ (99.5%) and KCl (99.5%) salts. The salts, $BaCO_3$ (99%) and TiO_2 (98%), were ball milled for 15 h. Then, the $Bi_4Ti_3O_{12}$ particles obtained in the first step were added and magnetically stirred with ethanol for 8 h. After drying, the mixture was calcined at 1040~1080 °C. An excess of $BaCO_3$ and TiO_2, equivalent to 10 mol% were added prior to the ball-milling process. Finally, $BaTiO_3$ was synthesized from the mixture of $BaBi_4Ti_4O_{15}$ and $BaCO_3$ (99%) with an equal weight of NaCl (99.5%) and KCl (99.5%) salts. The salts and $BaCO_3$ were ball milled, and then magnetic stirred with $BaBi_4Ti_4O_{15}$ particles for 8 h in ethanol. The mixture was dried at 90 °C. The calcined temperature was 925~975 °C. The heating rate was 4 °C/min throughout the calcination process. The salts of each step were removed by washing them several times in deionized water. Especially, in the third step, an acid-washing process was needed to remove the Bi_2O_3 byproduct. The calcined powder of the third step was washed in HNO_3 solution for 2 h, and then washed in deionized water several times.

2.2. Characterization

The phase structure was determined using a high-resolution X-ray diffractometer (XRD, PANalytical Empyrean, PANalytical, Almelo, the Netherlands) with Cu Kα1 radiation. The Raman spectra were collected by Raman spectrometer (RTS2-501-SMSXS, Zolix, Beijing, China) with a 532 nm laser at room temperature. The morphology of the $BaTiO_3$ and the precursor particles were examined using field-emission scanning electron microscopy (FE-SEM, FEI Quanta 250 FEG, FEI, Minato, Japan). Energy dispersive spectroscopic (EDS) mapping was carried out on the $BaTiO_3$ plates. A polarized light microscope (PLM, Olympus BX-51, Olympus, Tokyo, Japan) was used to investigate the extinction angle and the domain structure of the $BaTiO_3$. The domain structures of the $BaTiO_3$ plates were characterized by a piezoresponse force microscope (PFM, Dimension ICON, Bruker, Billerica, MA, USA).

3. Results and Discussion

The structure of Aurivilius compounds can be described as the intergrowth of $(Bi_2O_2)^{2+}$ layers and $(A_{n-1}B_nO_{3n+1})^{2-}$ layers, where n (n = 1–6) is the number of octahedral layers between two neighboring bismuth oxides layers [21]. Aurivilius-structured $Bi_4Ti_3O_{12}$ was chosen as the precursor, and was obtained by the reaction between Bi_2O_3 and TiO_2 according to Equation (1). In the second step of the TMC process, Ba^{2+} partially substituted Bi^{3+} in the $Bi_4Ti_3O_{12}$ precursor and formed $BaBi_4Ti_4O_{15}$ (Equation (2)). In the final step,

Ba^{2+} substituted all the residual Bi^{3+} in the $BaBi_4Ti_4O_{15}$, resulting in the formation of the final product $BaTiO_3$ (Equation (3)).

$$2Bi_2O_3 + 3TiO_2 \rightarrow Bi_4Ti_3O_{12} \quad (1)$$

$$Bi_4Ti_3O_{12} + BaCO_3 + 4TiO_2 \rightarrow BaBi_4Ti_4O_{15} + CO_2 \quad (2)$$

$$BaBi_4Ti_4O_{15} + BaCO_3 \rightarrow 2BaTiO_3 + 2Bi_2O_3 + CO_2 \quad (3)$$

Figure 1 shows the FE-SEM images of the $Bi_4Ti_3O_{12}$, $BaBi_4Ti_4O_{15}$ precursor particles and the $BaTiO_3$ plates synthesized at different temperatures. The results revealed that all the particles possess a plate-like shape. The morphology of the $Bi_4Ti_3O_{12}$ particles is shown in Figure 1a–c.

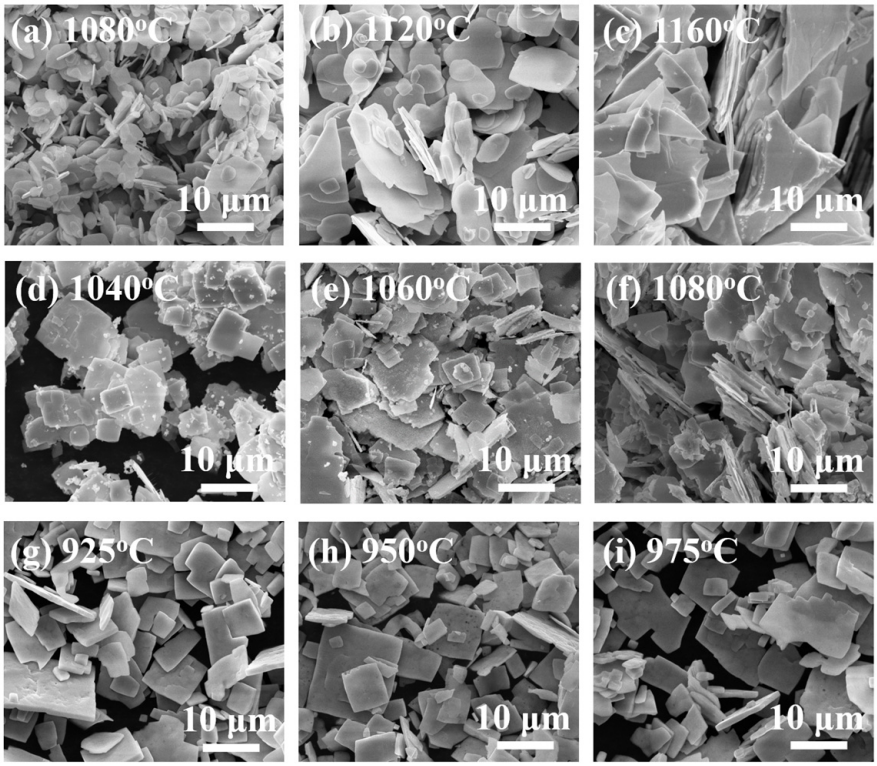

Figure 1. FE-SEM images of (**a**–**c**) $Bi_4Ti_3O_{12}$ precursor, (**d**–**f**) $BaBi_4Ti_4O_{15}$ precursor, and (**g**–**i**) $BaTiO_3$ mesoscale particles synthesized at different temperatures.

$BaBi_4Ti_4O_{15}$ nucleation initiates on the $Bi_4Ti_3O_{12}$ precursor and further grows by Ostwald ripening during the heating and holding stages. Generally, smaller particle size $Bi_4Ti_3O_{12}$ leads to smaller $BaBi_4Ti_4O_{15}$ after the topochemical reaction. Notably, the $Bi_4Ti_3O_{12}$ reaches a larger particle size at higher temperatures but shows obvious agglomeration in Figure 1c. The thickness of $Bi_4Ti_3O_{12}$ is about 0.2~1 μm. The length distributions are shown in Figure 2a–c. The average length of the $Bi_4Ti_3O_{12}$ synthesized at 1080 °C, 1120 °C, and 1160 °C are about 4.43 μm, 7.54 μm, and 12.51 μm, respectively. The $Bi_4Ti_3O_{12}$ obtained at 1080 °C in Figure 1a is too small and not suitable as a precursor. $Bi_4Ti_3O_{12}$ particles that grew at 1120 °C were selected as the precursor for the second step. $BaBi_4Ti_4O_{15}$ obtained at 1040 °C, 1060 °C, and 1080 °C are 6.23 μm, 7.73 μm, and 8.91 μm in length, respectively. The distribution curves show better uniformity at 1040 °C and 1060 °C temperature conditions, according to Figure 2d–f.

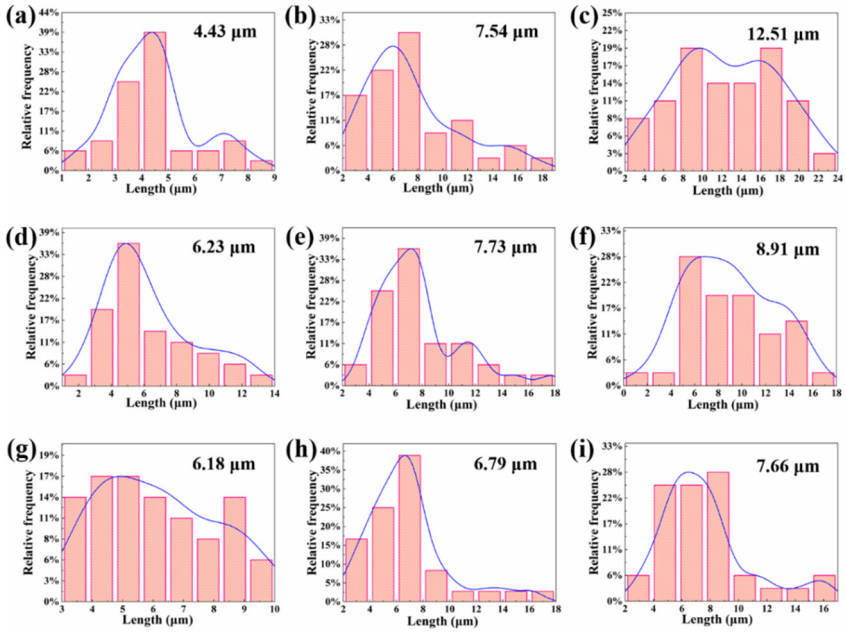

Figure 2. Length distributions of (**a**–**c**) $Bi_4Ti_3O_{12}$ precursor, (**d**–**f**) $BaBi_4Ti_4O_{15}$ precursor, and (**g**–**i**) $BaTiO_3$ mesoscale particles synthesized at different temperatures.

The FE-SEM images in Figure 1g–i show the plate-like shaped $BaTiO_3$ plates converted from the optimized $BaBi_4Ti_4O_{15}$ of the second step. The morphology of $BaTiO_3$ synthesized at 925 °C and 950 °C are similar. Figure 1g shows the $BaTiO_3$ synthesized at 925 °C with an average particle size of 6.18 μm. The particles possess suitable size in the range of 3–10 μm, but are not uniformly distributed. Moreover, the $BaTiO_3$ in Figure 1i contains many irregular shape particles with poor uniformity, which is also evidenced by Figure 2i. The $BaTiO_3$ plates obtained at 950 °C in Figure 1h are approximately 6.79 μm in length with a relatively regular square shape. The particles in Figure 1h are about 2~10 μm in length and about 0.5~1.3 μm in thickness. As shown in Figures 1h and 2h, the plates show good uniformity without obvious agglomeration. The products with the optimized condition of the three steps show no obvious changes in length between the precursors and $BaTiO_3$ plates, which means minimized exfoliation. These mesoscale $BaTiO_3$ particles exhibit a clean surface, and no obvious crack or hole was found. Note the obtained large anisotropic morphology and high aspect ratio are important for $BaTiO_3$ as templates in ceramic texturing applications. Moreover, the large specific surface area is also in favor of potential piezocatalysis applications.

Figure 3a shows the XRD patterns of the $BaTiO_3$ plates synthesized at 950 °C. Phase-pure $BaTiO_3$ particles were obtained. The diffraction pattern in Figure 3a can be well indexed with a standard PDF card (No. 81-2202) with a *P*4*mm* space group. Moreover, the lattice parameter of the $BaTiO_3$ plates is calculated to be a ≈ 4.00 Å and c ≈ 4.04 Å, which agree well with the reported value in standard PDF card, i.e., a = b = 3.99 Å, c = 4.04 Å. Figure 3b displays the Raman spectra measured in the frequency range of 100 cm^{-1} − 900 cm^{-1}. The inset is the photograph of the measured plate on a platinum substrate. The Raman spectra show peaks at 183 cm^{-1}, 301 cm^{-1}, 510 cm^{-1}, and 721 cm^{-1}, which is consistent with the literature [22–25]. The peak at ~180 cm^{-1} is related to the decoupling of the A_1(TO) phonons [19]. A weak peak at 301 cm^{-1} suggests the [B_1, E(TO + LO)] mode related to the TiO_6 octahedra [13,26]. The peaks at 510 cm^{-1} and 721 cm^{-1} correspond to the Raman active mode of [E(TO),A_1(TO)] and [E(LO),A_1(LO)], respectively.

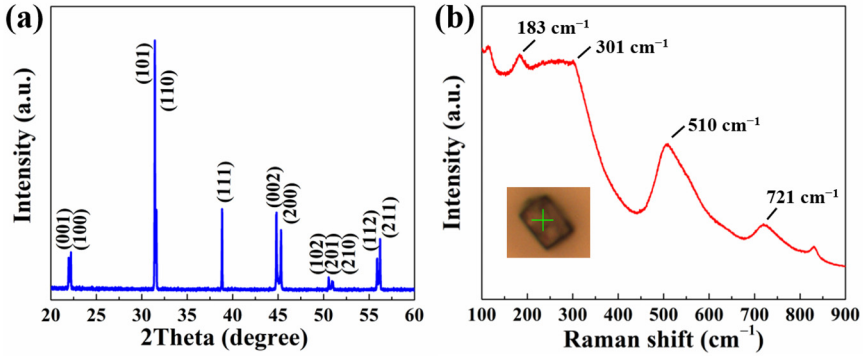

Figure 3. (**a**) XRD patterns and (**b**) the Raman spectra of $BaTiO_3$ plates synthesized at 950 °C. The inset in (**b**) indicates the measuring region in a single template with the light spot marked by a green cross.

Figure 4 exhibits the EDS mapping results on the surface of $BaTiO_3$ plates. The measured single plate is square in shape with a length of about 7 µm as shown in Figure 4a. The dotted lines in Figure 4b–d mark the boundary of the plate. Elements distribution of Ba, Ti, and O elements are shown in red, green, and yellow colors, respectively. Generally, Ba, Ti, and O elements are homogeneously distributed in the plates, suggesting good uniformity of the sample. Note in Figure 4d, a lower content of O elements was detected beyond the region of the plate, which may originate from the surrounding circumstance.

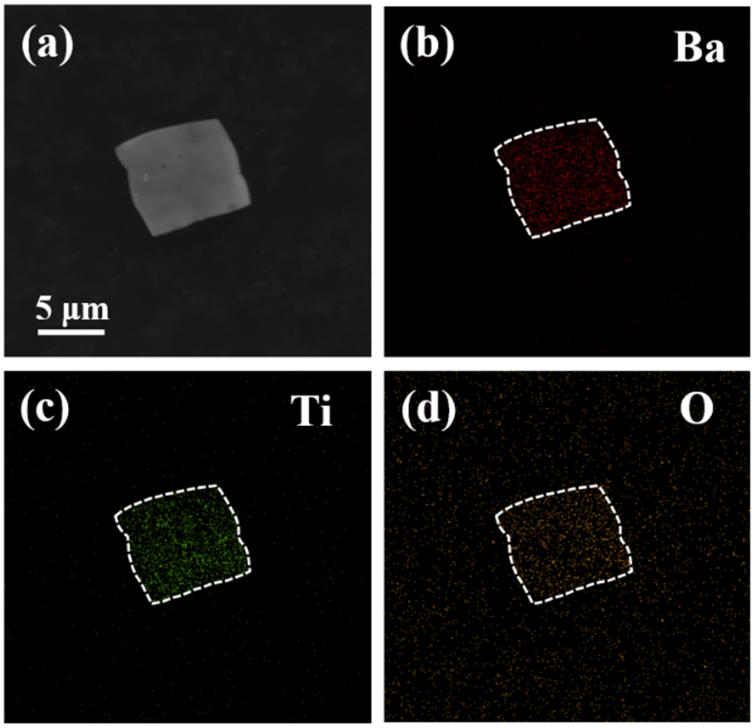

Figure 4. The EDS mapping results of the $BaTiO_3$ plates synthesized at 950 °C. (**a**) The FE-SEM image of the scanning area of EDS mapping includes a single $BaTiO_3$ plate. The distribution of (**b**) Ba element, (**c**) Ti element, and (**d**) O element in the scanning area.

PLM images of the (001) face of $BaTiO_3$ plates are depicted in Figure 5. The white arrow marks the direction of [100] along the edge of the $BaTiO_3$ plate. The images with crossed polarizer (P) and analyzer (A) are shown in Figure 5b–d at different intersection angles of 0°, 45°, and 90° between the analyzer and [100] direction. As shown in Figure 5b–d, the mesoscale $BaTiO_3$ plate reveals an extinction angle of 90 degrees, which is consistent with the tetragonal symmetry evidenced by XRD characterization in Figure 3. Moreover, the complete

extinction characteristics observed not only indicate the good uniformity of symmetry in the sample, but also suggest the unified orientation, i.e., the geometry of the template is coincident with the microscale perovskite unit cell. This also supports the single-crystal-like quality of the sample. The sample becomes color at 45° (the brightest position), reflecting the effect of *a*-domains in tetragonal $BaTiO_3$. However, no obvious regular domain patterns can be clearly seen. One possible reason is that the domain size is too small to be detected, as PLM cannot detect sub-micrometer scale domains. Another reason could be the domain overlapping, which may also make the PLM observation difficult.

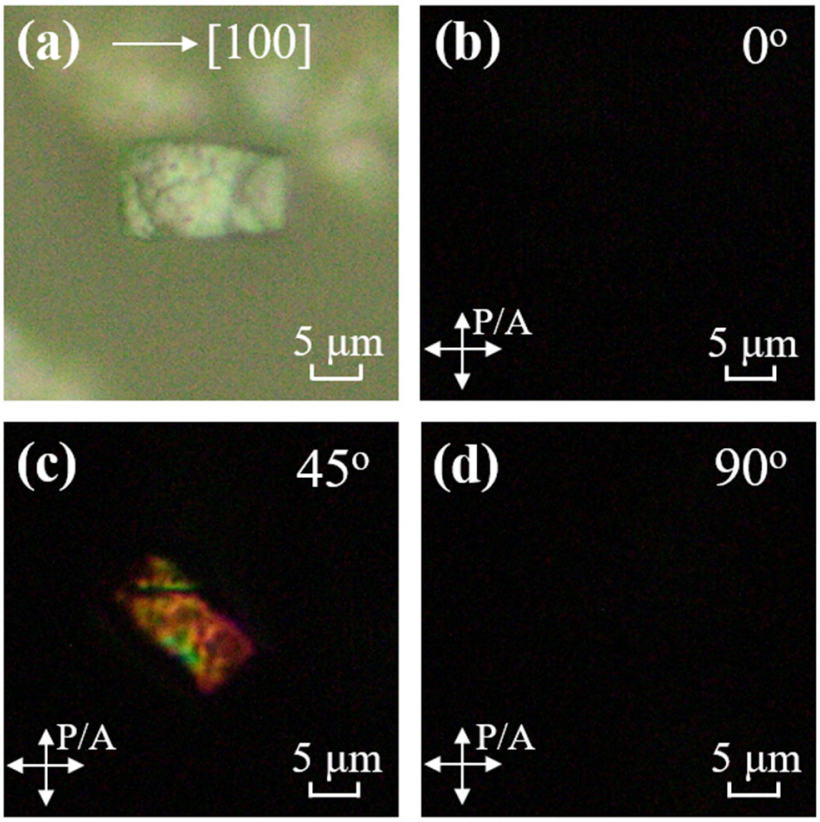

Figure 5. (**a**) The photograph of $BaTiO_3$ plates. The PLM images of $BaTiO_3$ micron plates with the crossed polarizers at (**b**) 0°, (**c**) 45°, and (**d**) 90°.

To further investigate the local domain structure in the micro-scale $BaTiO_3$ plates, PFM was performed on an individual plate. It can be seen that the out-of-plane as well as the in-plane amplitude images exhibit distinct contrast of about 180°, which is also revealed in the corresponding phase images. Figure 6a shows an out-of-plane PFM image recorded on the (001) surface of the plate, whereas the normal edge of the plate is oriented parallel to <001>-axis or <010>-axis. Figure 6c–f are the enlarged view of the region marked in Figure 6a. The roughness of this enlarged region extracted from the surface morphology image is ~43.5 nm. The rough surface is consistent with the FE-SEM results observed in Figures 1 and 4, which may be caused by the variation in growth rate in the different regions of the plate. Out-of-plane and in-plane images in the region of 6 μm × 6 μm area were recorded. The bright and dark stripes show the in-plane polarization with opposite directions along the <100>-axis (or <010>-axis), respectively. In the out-of-plane images, the bright and dark stripes indicate polarization with opposite directions along the <001>-axis. The $BaTiO_3$ plate shows a group of regular 90° ferroelectric banded domains with an average domain width of ~125 nm. In Figure 6b, a 3D schematic domain structure is sketched according to the possible orientation of the domains in the *T* phase (001) plate. Arrows indicate the orientation of spontaneous polarization (P_s). In the a_1/a_2-domain, the P_s is parallel with the surface of the plate, marked as P_1. In the *c*-domain, the P_s is perpendicular to the plate

surface, marked as P_2. The green stripes mark the *c*-domains while pink stripes represent the *a*-domains as illustrated in Figure 6b. The walls between 90° *a*/*c* domains intersect with the (001) plane by an angle of 45°. In the in-plane images, the bright and dark stripes correspond to P_1 and P_2, respectively. Meanwhile, in the out-of-plane images, the P_1 and P_2 regions also show distinct contrast. However, the bright and dark stripes indicate the P_2 and P_1, which are opposite to the in-plane signals. In previous studies, only irregularly shaped domain patterns were reported in mesoscale $BaTiO_3$ plates [19]. The results in Figure 6 show the first observation of typical 90° banded domains in such $BaTiO_3$ plates in mesoscale.

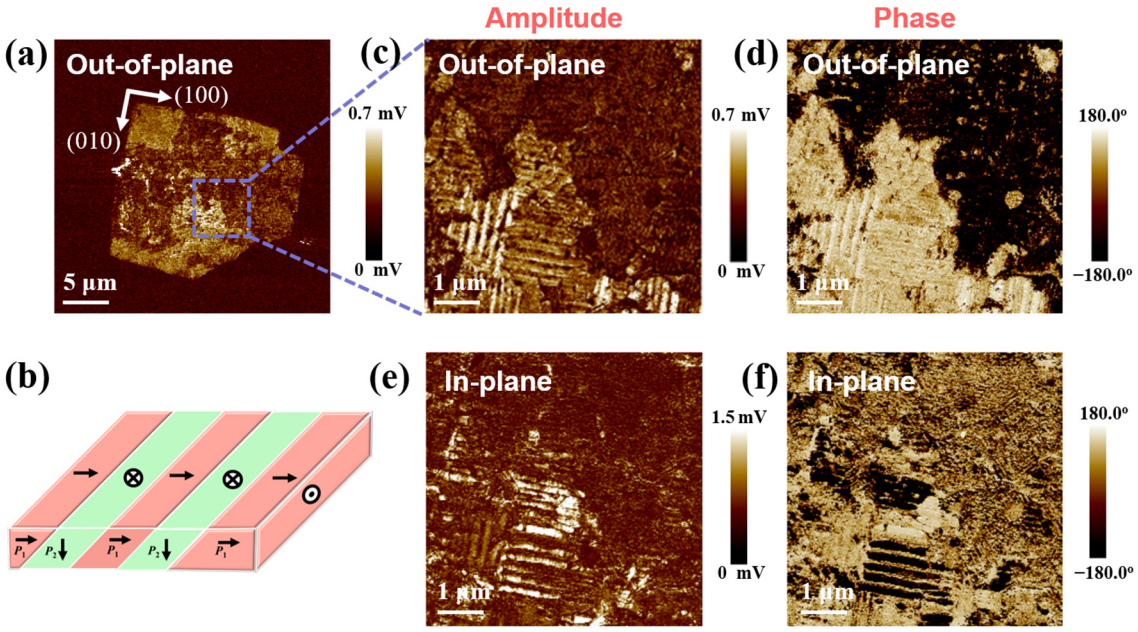

Figure 6. Domain structures of $BaTiO_3$ plate. (**a**) Out-of-plane PFM image of the whole plate. (**b**) 3D schematic domain structure. Out-of-plane (**c**) amplitude and (**d**) phase image, in-plane (**e**) amplitude, and (**f**) phase image of a 6 μm × 6 μm square region.

The features of the domain in mesoscale $BaTiO_3$ plates compared with bulk $BaTiO_3$ are worth further discussion. Different from the randomly oriented grains in $BaTiO_3$ ceramics, the $BaTiO_3$ plates possess a preferred orientation and much smaller sample thickness. The dimensions have a notable influence on the domain size. Though $BaTiO_3$ in the *T* phase is known to display typical 180° and 90° ferroelectric domain features [27], domain size can vary significantly with different microstructures. In the case of ceramics with different grain sizes, 90° domains of sub-micrometer scale were reported in the $BaTiO_3$ ceramics with 8.61 μm grains, whereas nanodomains (10~30 nm) were found in the ceramics of grain size <1 μm [28]. Also in $BaTiO_3$ single crystals, multiscale domain patterns covering a wide range from nanometers to several tenths of micrometers [29–31] are observed. Kittel's law shows the relation between the domain width w and the sample thickness t in ferroelectrics, ferromagnetics, and ferroelastics [32,33]. The domain width decreases with the decreasing thickness, i.e., $w^2 = kt$. The theoretical constant of proportionality k in this relation is reported to be 8.5×10^{-9} m for $BaTiO_3$ single crystals [34]. Adopted with the same parameter k, the calculated domain width w is in the range of 65~105 nm based on experimental thickness data. This is in the same order as our measured results ~125 nm, indicating the size dependence in mesoscale $BaTiO_3$ plate generally coincides with bulk single crystals.

4. Conclusions

The mesoscale plate-like $BaTiO_3$ was synthesized by the TMC technique in three steps. The $Bi_4Ti_3O_{12}$, $BaBi_4Ti_4O_{15}$ precursor, and the final product $BaTiO_3$ prepared at

different processing temperatures in each step were compared. The length distribution of the $Bi_4Ti_3O_{12}$, $BaBi_4Ti_4O_{15}$, and $BaTiO_3$ particles were analyzed based on the FE-SEM results. The dependence of morphology on synthesis conditions were discussed in detail. Micron-size plate-like $BaTiO_3$ plates with near square shape and high aspect ratio were obtained. The $BaTiO_3$ plates show good uniformity without obvious agglomeration. The average length of these (001) oriented plates is 6.79 μm. EDS results demonstrate the homogeneously distributed Ba, Ti, and O elements in the plates. XRD patterns, Raman spectra, and PLM results indicate that as-obtained $BaTiO_3$ plates possess a tetragonal phase structure at room temperature. Single-crystal-like extinction behavior and good uniformity are supported by PLM observations. The typical *a-c* domains are demonstrated by PFM, which is the first observation of typical 90° banded domains in such $BaTiO_3$ plates in mesoscale. The width of banded domains (~125 nm) generally satisfies Kittel's law of bulk single crystal. Moreover, there are regions with extremely weak signals in comparison with the banded 90° domain regions, which may have potential influences on applications used in the surface performance. The results may provide a new understanding of the domain structure of $BaTiO_3$ mesoscale materials and are helpful for promoting related applications.

Author Contributions: Conceptualization, J.Z. (Jian Zhuang), L.W. and W.R.; Methodology, K.Z. and Y.Q.; Formal analysis, Y.Q., J.Z. (Jinyan Zhao), L.W. and Z.W.; Investigation, K.Z., J.Z. (Jinyan Zhao) and L.W.; Resources, Z.W.; Writing—original draft, K.Z.; Writing—review and editing, J.Z. (Jian Zhuang) and W.R.; Funding acquisition, W.R. All authors have read and agreed to the published version of the manuscript.

Funding: This work was supported by the China National Key R&D Program (2021YFB3201800, 2020YFC0122100), Natural Science Foundation of China (Grants No. 12174299), Key Research Project of Shaanxi Province of China (Grant No. 2018ZDXM-GY-150), Xijiang Innovation Team Introduction Program of Zhaoqing (Jiecheng), China Postdoctoral Science Foundation (Grants No. 2019M663697), the "111 Project" of China (B14040), Funding from National Key Laboratory of Science and Technology on Space Microwave (HTKJ2021KL504015).

Institutional Review Board Statement: Not applicable.

Informed Consent Statement: Not applicable.

Data Availability Statement: Not applicable.

Conflicts of Interest: The authors declare that they have no known competing financial interest or personal relationships that could have appeared to influence the work reported in this paper.

References

1. Von Hippel, A. Ferroelectricity, Domain Structure, and Phase Transitions of Barium Titanate. *Rev. Mod. Phys.* **1950**, *22*, 221–237. [CrossRef]
2. Acosta, M.; Novak, N.; Rojas, V.; Patel, S.; Vaish, R.; Koruza, J.; Rossetti, G.A.; Rödel, J. $BaTiO_3$-Based Piezoelectrics: Fundamentals, Current Status, and Perspectives. *Appl. Phys. Rev.* **2017**, *4*, 041305. [CrossRef]
3. Wendari, T.P.; Arief, S.; Mufti, N.; Blake, G.R.; Baas, J.; Suendo, V.; Prasetyo, A.; Insani, A.; Zulhadjri, Z. Lead-Free Aurivillius Phase $Bi_2LaNb_{1.5}Mn_{0.5}O_9$: Structure, Ferroelectric, Magnetic, and Magnetodielectric Effects. *Inorg. Chem.* **2022**, *61*, 8644–8652. [CrossRef] [PubMed]
4. Janil Jamil, N.H.; Zainuddin, Z.; Hj Jumali, M.H.; Izzuddin, I.; Nadzir, L. Tetragonal Tungsten Bronze Phase Potential in Increasing the Piezoelectricity of Sol-Gel Synthesized $(K_{0.5}Na_{0.5})_{1-x}Li_xNbO_3$ Ceramics. *Ceram. Int.* **2022**, *48*, 9324–9329. [CrossRef]
5. Huang, C.; Wong-Ng, W.; Liu, W.F.; Zhang, X.N.; Jiang, Y.; Wu, P.; Tong, B.Y.; Zhao, H.; Wang, S.Y. Major Improvement of Ferroelectric and Optical Properties in Na-Doped Ruddlesden-Popper Layered Hybrid Improper Ferroelectric Compound, $Ca_3Ti_2O_7$. *J. Alloys Compd.* **2019**, *770*, 582–588. [CrossRef]
6. Zhang, J.; Wang, C.; Bowen, C. Piezoelectric Effects and Electromechanical Theories at the Nanoscale. *Nanoscale* **2014**, *6*, 13314–13327. [CrossRef]
7. Liu, S.; Wang, L.; Feng, X.; Wang, Z.; Xu, Q.; Bai, S.; Qin, Y.; Wang, Z.L. Ultrasensitive 2D ZnO Piezotronic Transistor Array for High Resolution Tactile Imaging. *Adv. Mater.* **2017**, *29*, 1606346. [CrossRef] [PubMed]
8. Qian, W.; Zhao, K.; Zhang, D.; Bowen, C.R.; Wang, Y.; Yang, Y. Piezoelectric Material-Polymer Composite Porous Foam for Efficient Dye Degradation via the Piezo-Catalytic Effect. *ACS Appl. Mater. Interfaces* **2019**, *11*, 27862–27869. [CrossRef]
9. Choi, W.; Choudhary, N.; Han, G.H.; Park, J.; Akinwande, D.; Lee, Y.H. Recent Development of Two-Dimensional Transition Metal Dichalcogenides and Their Applications. *Mater. Today* **2017**, *20*, 116–130. [CrossRef]

10. Messing, G.L.; Poterala, S.; Chang, Y.; Frueh, T.; Kupp, E.R.; Watson, B.H.; Walton, R.L.; Brova, M.J.; Hofer, A.K.; Bermejo, R.; et al. Texture-Engineered Ceramics - Property Enhancements through Crystallographic Tailoring. *J. Mater. Res.* **2017**, *32*, 3219–3241. [CrossRef]
11. Moriana, A.D.; Zhang, S. Lead-Free Textured Piezoceramics Using Tape Casting: A Review. *J. Mater.* **2018**, *4*, 277–303. [CrossRef]
12. Kalhori, H.; Amaechi, I.C.; Youssef, A.H.; Ruediger, A.; Pignolet, A. Catalytic Activity of $BaTiO_3$ Nanoparticles for Wastewater Treatment: Piezo- or Sono-Driven? *ACS Appl. Nano Mater.* **2022**, *6*, 1686–1695. [CrossRef]
13. Tang, Q.; Wu, J.; Kim, D.; Franco, C.; Terzopoulou, A.; Veciana, A.; Puigmartí-Luis, J.; Chen, X.Z.; Nelson, B.J.; Pané, S. Enhanced Piezocatalytic Performance of $BaTiO_3$ Nanosheets with Highly Exposed {001} Facets. *Adv. Funct. Mater.* **2022**, *32*, 2–9. [CrossRef]
14. Remeika, J.P. A Method for Growing Barium Titanate Single Crystals. *J. Am. Chem. Soc.* **1954**, *76*, 940–941. [CrossRef]
15. Merz, W.J. Double Hysteresis Loop of $BaTiO_3$ at the Curie Point. *Phys. Rev.* **1953**, *91*, 513–517. [CrossRef]
16. Liu, D.; Yan, Y.; Zhou, H. Synthesis of Micron-Scale Platelet $BaTiO_3$. *J. Am. Ceram. Soc.* **2007**, *90*, 1323–1326. [CrossRef]
17. Poterala, S.F.; Chang, Y.; Clark, T.; Meyer, R.J.; Messinge, G.L. Mechanistic Interpretation of the Aurivillius to Perovskite Topochemical Microcrystal Conversion Process. *Chem. Mater.* **2010**, *22*, 2061–2068. [CrossRef]
18. Hao, M.; Fan, G.; Lou, Y.; Wen, Y.; Deng, H.; Wang, F.; Lv, W.; Yuchi, M.; Ding, M. Regular and Uniform-Shaped $BaTiO_3$ Microplates Prepared Using a Modified Precursor. *Ceram. Int.* **2019**, *45*, 2338–2344. [CrossRef]
19. Kržmanc, M.M.; Jančar, B.; Uršič, H.; Tramšek, M.; Suvorov, D. Tailoring the Shape, Size, Crystal Structure, and Preferential Growth Orientation of $BaTiO_3$ Plates Synthesized through a Topochemical Conversion Process. *Cryst. Growth Des.* **2017**, *17*, 3210–3220. [CrossRef]
20. Su, S.; Zuo, R.; Lv, D.; Fu, J. Synthesis and Characterization of (001) Oriented $BaTiO_3$ Platelets through a Topochemical Conversion. *Powder Technol.* **2012**, *217*, 11–15. [CrossRef]
21. Aurivillius, B. Mixed bismuth oxides with layer lattices: I. The structure type of $CaNb_2Bi_2O_9$. *Ark. For. Kemi.* **1949**, *1*, 463–480.
22. Pinczuk, A.; Taylor, W.; Burstein, E.; Lefkowitz, I. The Raman Spectrum of $BaTiO_3$. *Solid State Commun.* **1967**, *5*, 429–433. [CrossRef]
23. Huang, L.; Chen, Z.; Wilson, J.D.; Banerjee, S.; Robinson, R.D.; Herman, I.P.; Laibowitz, R.; O'Brien, S. Barium Titanate Nanocrystals and Nanocrystal Thin Films: Synthesis, Ferroelectricity, and Dielectric Properties. *J. Appl. Phys.* **2006**, *100*, 034316. [CrossRef]
24. Kharat, S.P.; Gaikwad, S.K.; Nalam, P.G.; Kambale, R.C.; James, A.R.; Kolekar, Y.D.; Ramana, C.V. Effect of Crystal Structure and Phase on the Dielectric, Ferroelectric, and Piezoelectric Properties of Ca^{2+}- and Zr^{4+}-Substituted Barium Titanate. *Cryst. Growth Des.* **2022**, *22*, 5571–5581. [CrossRef]
25. Xu, K.; Zhu, G.; Xu, H.; Zhao, Y.; Jiang, K.; Zhang, X.; Yin, H.; Shangguan, M.; Wan, L.; Huang, T. The Colossal Permittivity Effect on $BaTiO_3$ Induced by Different Sinter Atmosphere. *Appl. Phys. A* **2022**, *128*, 1044. [CrossRef]
26. Pugachev, A.M.; Zaytseva, I.V.; Surovtsev, N.V.; Krylov, A.S. Anharmonicity and Local Noncentrosymmetric Regions in $BaTiO_3$ Pressed Powder Studied by the Raman Line Temperature Dependence. *Ceram. Int.* **2020**, *46*, 22619–22623. [CrossRef]
27. Tagantsev, A.K.; Cross, L.E.; Fousek, J. *Domains in Ferroic Crystals and Thin Films*; Springer: New York, NY, USA, 2010.
28. Huan, Y.; Wang, X.; Fang, J.; Li, L. Grain Size Effects on Piezoelectric Properties and Domain Structure of $BaTiO_3$ Ceramics Prepared by Two-Step Sintering. *J. Am. Ceram. Soc.* **2013**, *96*, 3369–3371. [CrossRef]
29. McQuaid, R.G.P.; McGilly, L.J.; Sharma, P.; Gruverman, A.; Gregg, J.M. Mesoscale Flux-Closure Domain Formation in Single-Crystal $BaTiO_3$. *Nat. Commun.* **2011**, *2*, 404. [CrossRef]
30. Howell, J.A.; Vaudin, M.D.; Cook, R.F. Orientation, Stress, and Strain in an (001) Barium Titanate Single Crystal with 90° Lamellar Domains Determined Using Electron Backscatter Diffraction. *J. Mater. Sci.* **2014**, *49*, 2213–2224. [CrossRef]
31. McGilly, L.; Byrne, D.; Harnagea, C.; Schilling, A.; Gregg, J.M. Imaging Domains in $BaTiO_3$ Single Crystal Nanostructures: Comparing Information from Transmission Electron Microscopy and Piezo-Force Microscopy. *J. Mater. Sci.* **2009**, *44*, 5197–5204. [CrossRef]
32. Kittel, C. Theory of the Structure of Ferromagnetic Domains in Films and Small Particles. *Phys. Rev.* **1946**, *70*, 965–971. [CrossRef]
33. Kittel, C. Physical theory of ferromagnetic domains. *Rev. Mod. Phys.* **1949**, *21*, 541. [CrossRef]
34. Schilling, A.; Adams, T.B.; Bowman, R.M.; Gregg, J.M.; Catalan, G.; Scott, J.F. Scaling of Domain Periodicity with Thickness Measured in $BaTiO_3$ Single Crystal Lamellae and Comparison with Other Ferroics. *Phys. Rev. B-Condens. Matter Mater. Phys.* **2006**, *74*, 1–6. [CrossRef]